Using Burst Excitation to obtain Acoustic Material Properties in Impedance Tubes

Felix Huber[1], Semere Birhane Gebrekidan[1], Maximilian Lösch[1], Florian Toth[1]

[1] *TU Wien, Institute of Mechanics and Mechatronics, 1060 Vienna, Austria, Email: felix.huber@tuwien.ac.at*

Motivation

State-of-the-art acoustic research often relies heavily on complex signal processing to extract the required information. For certain problems, burst signals provide a simple and intuitive method for analyzing complex acoustic structures. One example is the investigation of topology-optimized wave guides [1]. Despite the clear advantage of short signals - allowing for the visualization of wave propagation - wave decomposition can be simplified using the time domain approach presented in this paper. Furthermore, the burst signals allow measurements of non-steady-state properties, enabling investigation of the settling process and nonlinearities, both of which would extend the presented methods.

Methods

To maintain comparability with the standardized and well-established four-microphone method [2], the proposed method alters only the wave composition step by computing the decomposition in the time domain. The setup is sketched in Figure 1. We exploit the short burst with tube lengths

$$L_\mathrm{u} = L_\mathrm{d} \gg T_\mathrm{burst} c_0 \tag{1}$$

which enable a spacial wave decomposition for the burst duration T_burst and the speed of sound c_0. To deal with

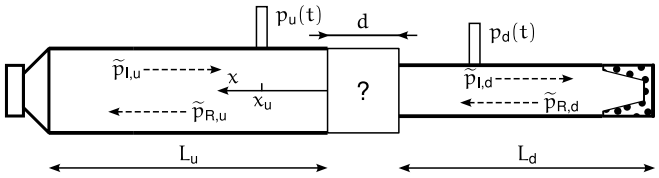

Figure 1: Experimental setup for the burst method with diameter-reducing air-filled structures inserted at ?.

the overlapping incident and reflected waves in the upstream tube, we first record a reference signal in an empty straight tube and subtract it from the recorded signal of our measurement setup, similar to the standardized subtraction method [3]. Alternatively, the length of the upstream tube could be doubled to enable true time domain wave decomposition without a reference measurement.

The complex decomposed wave pressures for the upstream and downstream tube can be computed as

$$\widetilde{p}_\mathrm{I,u} = \mathcal{F}_w \left\{ p_\mathrm{u,ref}\left(t - \frac{x_\mathrm{u}}{c_0}\right)\right\} , \tag{2}$$

$$\widetilde{p}_\mathrm{R,u} = \mathcal{F}_w \left\{ p_\mathrm{u}\left(t + \frac{x_\mathrm{u}}{c_0}\right) - p_\mathrm{u,ref}\left(t + \frac{x_\mathrm{u}}{c_0}\right)\right\} \text{ and} \tag{3}$$

$$\widetilde{p}_\mathrm{I,d} = \mathcal{F}_w \left\{ p_\mathrm{d}\left(t - \frac{x_\mathrm{d}}{c_0}\right)\right\} , \tag{4}$$

with the centrally windowed, and symmetrically padded Fourier transform denoted $\mathcal{F}_w$ and the respective microphone positions x_u and x_d. Given the length constraints of the downstream tube, the reflected downstream pressure $\widetilde{p}_\mathrm{R,d}$ can be assumed to be zero.

Finally, the material parameters for reflection $\widetilde{r}$, transmission $\widetilde{\tau}$ and absorption α can be obtained by

$$\widetilde{r} = \frac{\widetilde{p}_\mathrm{R,u}}{\widetilde{p}_\mathrm{I,u}} , \tag{5}$$

$$\widetilde{\tau} = \frac{\widetilde{p}_\mathrm{I,d}}{\widetilde{p}_\mathrm{I,u}} \frac{r_\mathrm{d}}{r_\mathrm{u}} \text{ and} \tag{6}$$

$$\alpha = 1 - \widetilde{r}\widetilde{r}^* - \widetilde{\tau}\widetilde{\tau}^* , \tag{7}$$

with $\square^*$ denoting the complex conjugate and the respective upstream and downstream radii r_u and r_d. These simplified definitions are equivalent to the transfer matrix method for geometrically symmetric samples [2].

The four burst signals used in this paper are given by

$$f_\mathrm{sinc} = \frac{\sin(\omega\hat{t})}{\omega\hat{t}} e^{-\alpha(\omega\hat{t})^2} , \tag{8}$$

$$f_\mathrm{gauss} = e^{-(\omega\hat{t})^2} , \tag{9}$$

$$f_\mathrm{hermite} = 2\omega\hat{t} e^{-0.5(\omega\hat{t})^2} \text{ and} \tag{10}$$

$$f_\mathrm{ricker} = \left[1 - (\omega\hat{t})^2\right] e^{-0.5(\omega\hat{t})^2} , \tag{11}$$

with the angular frequency $\omega = 2\pi \cdot 5000\,\mathrm{Hz}$ and the shifted time $\hat{t} = t - t_\mathrm{center}$ where $t_\mathrm{center} = 0.5\,\mathrm{ms}$. The evaluated functions and their frequency content are shown in Figure 2.

Simulation

To verify the proposed methods, the setup in Figure 1 is modeled as an axisymmetric Finite Element Method (FEM) problem with the dimensions $r_\mathrm{u} = 25\,\mathrm{mm}$, $r_\mathrm{d} = 15\,\mathrm{mm}$ and $L_\mathrm{u} = L_\mathrm{sample} = L_\mathrm{d} = 100\,\mathrm{mm}$. The air-filled structures are defined by a stepped and a linear diameter decrease. The resulting meshes are shown in Figure 3. Perfectly Matched Layers (PMLs) are used to absorb reflected and transmitted waves. The excitation is modeled as a normal velocity boundary condition between the input PML and the acoustic domain, resulting in a non-reflective ("invisible") excitation.

Second order elements are used and the problem is solved in the frequency domain for the four-microphone reference solution and in the time domain for the introduced burst signal method. We use the open-source FEM solver openCFS [4] to solve the stated problem, while Python is used for post-processing.

Except for minor low-frequency phase deviations, the results for the stepped geometry in Figure 4 show a near-

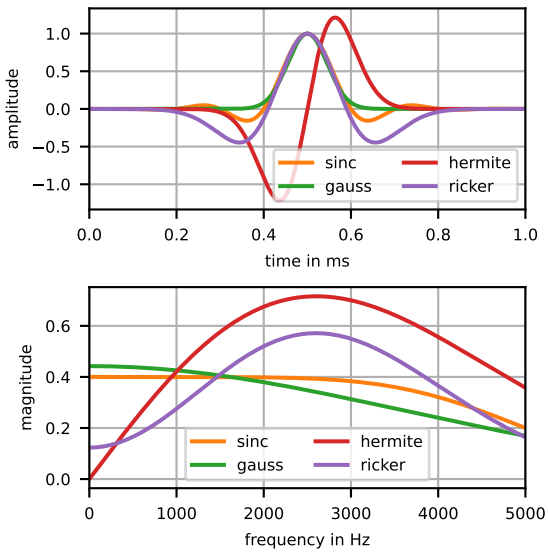

Figure 2: Time domain evaluation of the burst signals (top) and their respective frequency content obtained by padded Fourier transformation (bottom).

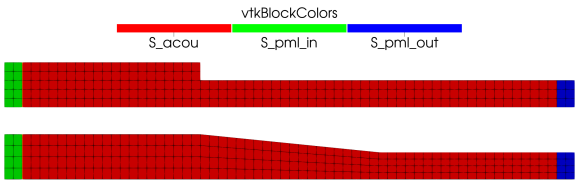

Figure 3: FEM mesh for the stepped structure (top) and the linear structure (bottom) with PMLs at input and output.

perfect match. These deviations are expected due to the low spectral content of the Hermite signal at low frequencies.

The results for the linear structure, shown in Figure 5, did not match as closely as those for the stepped geometry. This discrepancy is caused by the low spectral information in the 1 ms pulse, which results in a frequency resolution of $\Delta f = 1/T_{\text{burst}} = 1000\,\text{Hz}$. Although to the padded Fourier transform improves the visual resolution, the resulting phase still lacks sufficient detail to fully reconstruct the phase gradient caused by late reflections in the extended structure. This reduced resolution is the main drawback of the burst method, which should be considered when interpreting the results.

Experiments

To assess the practical applicability of the burst method, a modular impedance tube is used. The tube is constructed from aluminum tubes combined with 3D-printed parts, as shown in Figure 6. The structures under test are printed from Polyethylenterephthalat (PETG).

For the acoustic measureent, MEMS-based microphones [6] are combined with the RME Fireface UFX+ interface and connected to a PC. The open-source Python package ASMU [5] is used to generate, record and process the signals in real time, enabling fast and high precision measurements.

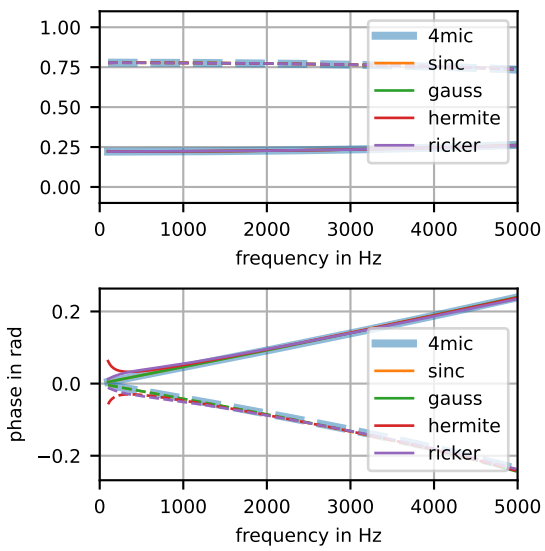

Figure 4: Simulation results for the stepped structure, showing reflection (solid) and transmission (dashed) coefficients. Comparison of the four bursts with the four-microphone (4mic) reference solution. Squared magnitude (top) and phase angle (bottom).

Signal reproduction

Prior to the measurements, we assess the producibility of the given burst signals. The speaker used (Visaton FRS 8 M) has issues producing the short burst signals due to its inherent dynamics between the output pressure and input voltage. The problem is illustrated by the solid lines in Figure 8, shown as an example for the gauss burst.

To overcome this limitation, a speaker model (SM) was derived from the Thiele-Small parameters given by the manufacturer. The problem is sketched in Figure 7 and can be described by the linear state-space model

$$\frac{\partial}{\partial t}\underbrace{\begin{bmatrix} I \\ q \\ \frac{\partial q}{\partial t} \end{bmatrix}}_{\boldsymbol{x}} = \underbrace{\begin{bmatrix} -\frac{R}{L} & 0 & 0 \\ 0 & 0 & 1 \\ \frac{Bl}{m} & -\frac{k}{m} & -\frac{c}{m} \end{bmatrix}}_{\boldsymbol{A}} \underbrace{\begin{bmatrix} I \\ q \\ \frac{\partial q}{\partial t} \end{bmatrix}}_{\boldsymbol{x}} + \underbrace{\begin{bmatrix} \frac{q}{L} \\ 0 \\ 0 \end{bmatrix}}_{\boldsymbol{b}} u\,, \tag{12}$$

$$y = \underbrace{\begin{bmatrix} 0 & 0 & \rho_0 c_0 \end{bmatrix}}_{\boldsymbol{c}^\intercal} \underbrace{\begin{bmatrix} I \\ q \\ \frac{\partial q}{\partial t} \end{bmatrix}}_{\boldsymbol{x}}\,, \tag{13}$$

with the total resistance $R = R_L + R_{amp}$ and the membrane stiffness k calculated by

$$k = \left(\frac{V_{\text{as}}}{\rho_0 c_0^2 S_d^2}\right)^{-1}\,, \tag{14}$$

with the equivalent volume V_{as} and the effective piston area S_d. The model poles are stable, and the states show full observability and controllability.

To enforce an arbitrary signal on the output of the system, a feedforward control law based on the input-output dynamics can be implemented as

$$u_{\text{ideal}} = [\boldsymbol{c}^\intercal \boldsymbol{A}\boldsymbol{b}]^{-1}\left[\frac{\partial^2}{\partial t^2} y_{\text{d}} - \boldsymbol{c}^\intercal \boldsymbol{A}^2 \boldsymbol{x}_{\text{d}}\right]\,. \tag{15}$$

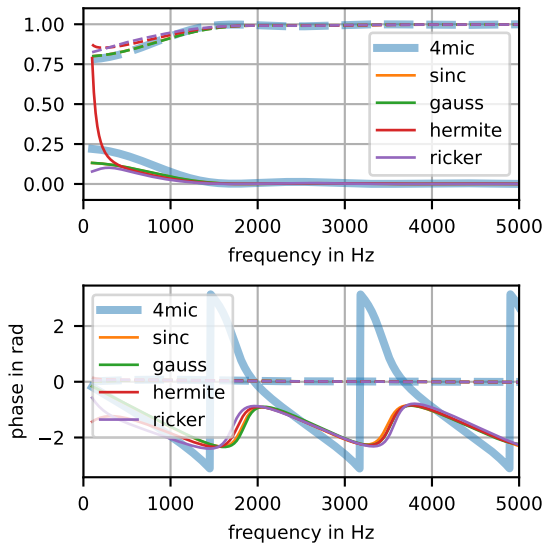

Figure 5: Simulation results for the linear structure, showing reflection (solid) and transmission (dashed) coefficients. Comparison of the four bursts with the four-microphone (4mic) reference solution. Squared magnitude (top) and phase angle (bottom).

Figure 6: Measurement setup for the reference tube (top) and the diameter change (bottom).

To obtain the desired state vector $\boldsymbol{x}_\mathrm{d}$ from the desired output y_d, the state transformation $\boldsymbol{T}$ is introduced as

$$\boldsymbol{z}_\mathrm{d} = \begin{bmatrix} y_\mathrm{d} \\ \frac{\partial}{\partial t} y_\mathrm{d} \\ z_3 \end{bmatrix} = \underbrace{\begin{bmatrix} \boldsymbol{c}^\mathsf{T} \\ \boldsymbol{c}^\mathsf{T}\boldsymbol{A} \\ \boldsymbol{t}_3^\mathsf{T} \end{bmatrix}}_{\boldsymbol{T}} \boldsymbol{x}_\mathrm{d} \,, \tag{16}$$

which must be invertible. However, as the system exhibits a non-full relative degree, caused by the system order being different from the order of input-output dynamics, the system has internal dynamics. These are described by z_3, which connects to the original system dynamics by $\boldsymbol{t}_3^\mathsf{T} = \begin{bmatrix} 0 & 1 & 1 \end{bmatrix}$, chosen such that $\boldsymbol{t}_3^\mathsf{T}\boldsymbol{b} = 0$ to ensure the internal dynamics are independent of the input. Hence for a given y_d, the internal dynamics can be solved with

$$\frac{\partial}{\partial t} z_3 = \boldsymbol{t}_3^\mathsf{T} \boldsymbol{A} \boldsymbol{T}^{-1} \begin{bmatrix} y_\mathrm{d} \\ \frac{\partial}{\partial t} y_\mathrm{d} \\ z_3 \end{bmatrix} \,. \tag{17}$$

By inserting z_3 into the inverted transformation obtained by Equation (16) we obtain $\boldsymbol{x}_\mathrm{d}$, which is used in Equation (15) to obtain u_ideal. For a more detailed explanation the reader is referred to Lunze [7].

It must be noted, that for implementing this feedforward control law the desired output trajectory y_d must be at least twice differentiable. As initial conditions, the trajectory and its derivatives should be zero at the start and end of the signal, since nonzero values would imply physically impractical conditions.

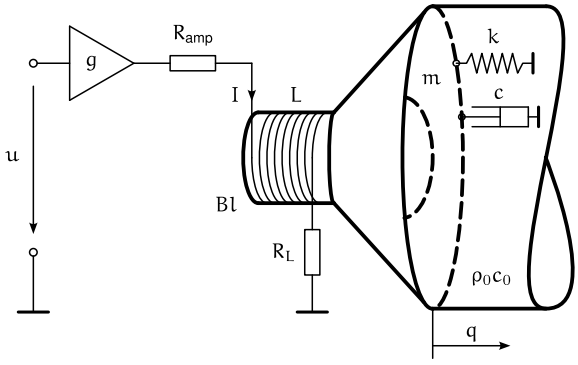

Figure 7: Speaker model

The model accuracy is shown by the solid gray line in Figure 8 and the trajectory control for both the model and pressure measurements shows good agreement. The small pressure oscillations after the trajectory-controlled burst are most likely caused by reflections in the speakers inlet funnel, which is not modelled in the proposed state-space model. Due to the lack of feedback, the controller is prone to model errors and disturbances.

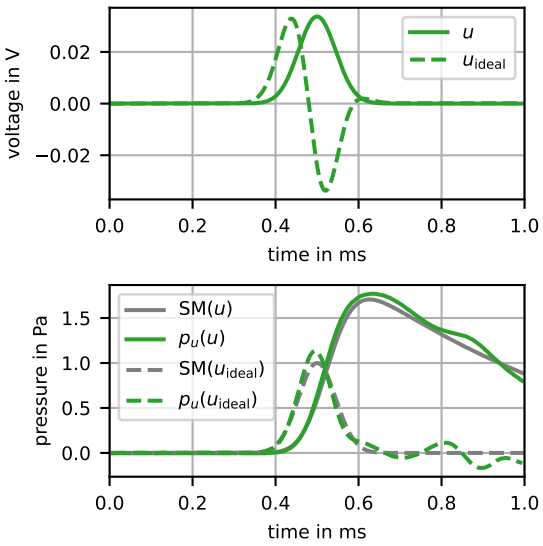

Figure 8: Scaled original burst signal u (solid, top) for the gauss burst, along with its speaker model response (SM) and measured response (solid, bottom), compared to the feedforward controller signal u_ideal (dashed, top) and its respective responses (dashed, bottom).

Material parameters

Finally, the trajectory controlled voltage signals are used to excite the pressure bursts inside the tube. The FEM result of the sinc is used as the reference because it proved to be the most accurate. The burst method is used to analyze the recorded signals, and the results are compared in Figure 9 for the stepped structure and in Figure 10

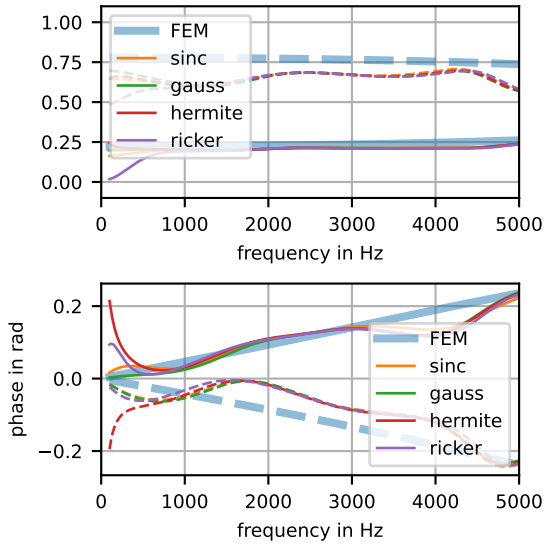

Figure 9: Experimental results for the stepped structure, showing reflection (solid) and transmission (dashed) coefficients. Comparison of the four bursts with the sinc simulation (FEM).

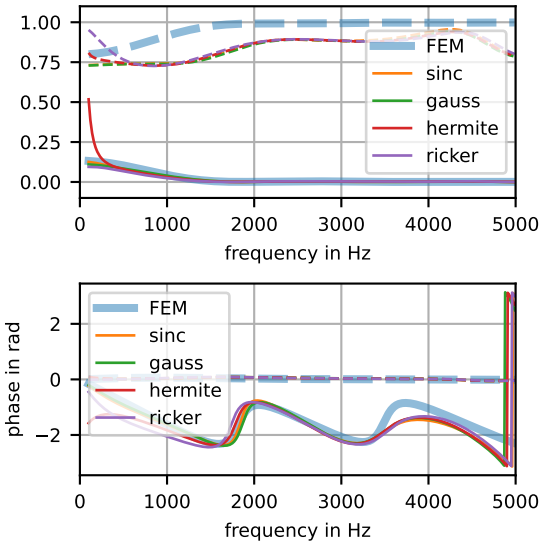

Figure 10: Experimental results for the linear structure, showing reflection (solid) and transmission (dashed) coefficients. Comparison of the four bursts with the sinc simulation (FEM).

for the linear structure. All results represent the average of ten measurements to ensure reliability and reduce random variations, with only minor deviations observed between individual measurements.

The reflection coefficients show excellent agreement, despite the known low-frequency and resolution problems. The transmission coefficient has decreased significantly, which can be explained by losses caused by the thin-walled hollow 3D-printed structures. The absorption coefficient is omitted from visualization, as it directly corresponds to the difference between the lossless FEM and the respective burst signal.

Conclusion

Because of the conformity to the standardized four-microphone method, the introduced burst method performed well and successfully produced comparable results. By selecting burst functions with good spectral coverage, numerical errors can be minimized. A remaining challenge is the low-frequency resolution caused by the short burst signal. The applied padding did not suffice to accurately replicate the phase gradient of the reference measurement.

For future research, signal processing techniques could be improved to enhance frequency resolution. Cross-correlation may also serve as a powerful tool for addressing these kind of signal processing challenges. More rigid structures, such as solid-infill designs, should be investigated to assess their impact on absorption properties and reinforce the current argumentation. Furthermore, the proposed feedforward controller could be extended and tuned with measurement data to eliminate the small remaining oscillations, potentially improving the overall system performance.

References

[1] Mousavi, A., Berggren, M., Hägg, L., Wadbro, E., 2024. Topology optimization of a waveguide acoustic black hole for enhanced wave focusing. The Journal of the Acoustical Society of America 155, 742–756. https://doi.org/10.1121/10.0024470

[2] ASTM International, 2019. ASTM E2611-19 Standard Test Method for Normal Incidence Determination of Porous Material Acoustical Properties Based on the Transfer Matrix Method. https://doi.org/10.1520/E2611-19

[3] International Organization for Standardization, 2022. ISO 13472-1:2022 Acoustics - Measurement of sound absorption properties of road surfaces in situ - Part 1: Extended surface method.

[4] openCFS. https://opencfs.org

[5] Acoustic Signal Measurement Utilities (ASMU). https://pypi.org/project/asmu/

[6] Huber, F., Toth, F., 2025. MEMS measurement microphone compatible to P48 amplifiers. HardwareX 21, e00627. https://doi.org/10.1016/j.ohx.2025.e00627

[7] Lunze, J., 2020. Regelungstechnik 1: Systemtheoretische Grundlagen, Analyse und Entwurf einschleifiger Regelungen. Springer Berlin Heidelberg, Berlin, Heidelberg. https://doi.org/10.1007/978-3-662-60746-6